INTERNATIONAL JOURNAL FOR NUMERICAL METHODS IN FLUIDS
*Int. J. Numer. Meth. Fluids* 2004; **45**:1317–1338 (DOI: 10.1002/fld.740)

# Large eddy simulation of turbulent concentric annular channel flows

Nan-Sheng Liu and Xi-Yun Lu*,†

*Department of Modern Mechanics, University of Science and Technology of China, Hefei, Anhui 230026, People's Republic of China*

SUMMARY

Fully developed turbulent concentric annular channel flow has been investigated numerically by use of large eddy simulation (LES) technique coupled with a localized one-equation dynamic subgrid-scale (SGS) model. The objective of this study is to deal with the behaviour of turbulent flow near the inner and outer walls of the concentric annular channel and to examine the effectiveness of LES technique for predicting the turbulent flow influenced by the transverse curvature effect. The computations are performed for the Reynolds number $Re_\tau = 180$, 395 and 640, based on an averaged friction velocity and the annular channel width with the inner and outer cylinder radius being $R_i = 1$ and $R_o = 2$. To validate the present approach, calculated results for turbulent pipe flow and concentric annular channel flow are compared with available experimental data and direct numerical simulation results, which confirms that the present approach can be used to study turbulent concentric annular channel flow satisfactorily. To elucidate turbulence characteristics in the concentric annular channel, some typical quantities, including the resolved velocity, turbulence intensity, turbulent eddy viscosity, SGS kinetic energy, SGS dissipation rate, Reynolds stress budgets, and turbulence structures based on the velocity fluctuations, are analysed.


KEY WORDS: large eddy simulation (LES); subgrid-scale (SGS) model; localized dynamic model; concentric annular channel flow; turbulent flow

## 1. INTRODUCTION

Turbulent flow in a concentric annular channel is of great importance because of its extensive applications in engineering, for example, heat exchangers, nuclear reactor cores, combustion

*Correspondence to: Prof. Xi-Yun Lu, Department of Modern Mechanics, University of Science and Technology of China, Hefei, Anhui 230026, People's Republic of China.
†E-mail: xlu@ustc.edu.cn

Contract/grant sponsor: National Natural Science Foundation of China; contract/grant numbers: 10302028, 10125210
Contract/grant sponsor: Chinese Academy of Sciences
Contract/grant sponsor: Specialized Research Fund for the Doctoral Program of Higher Education; contract/grant number: 20020358013

Published online 25 May 2004
*Received 23 December 2003*
*Revised 29 March 2004*

systems. Some work has been done to understand the characteristics of such turbulent flow and to model the flow field for the design of more efficient equipment. Usually, flow in a parallel channel generates a symmetrical velocity profile and makes the positions of zero shear stress and maximum velocity coincident. However, the flow in a concentric annular channel is an asymmetric flow. The asymmetric velocity profiles result from the interaction of two flow zones with different Reynolds numbers based on the outer and inner cylinder radius, respectively. The transverse curvature alters significantly the overall characteristics of the wall bounded turbulence structure in the vicinity of the inner and outer walls when changing the radius ratio $\alpha = R_i/R_o$ with $R_i$ and $R_o$ being the inner and outer cylinder radius. It is expected that turbulent transport phenomena in asymmetric flows differ from those in symmetrical flows.

Some experiments on annular channel turbulence have been performed because of the simplicity of the geometry. Brighton [1] and Brighton and Jones [2] measured turbulence intensities and shear stresses. Lawn and Elliott [3] dealt with experimentally turbulent annular channel flows with three different radius ratios to reveal the effect of the radius ratio on the annular channel flow. Rehme [4] investigated the turbulence in the concentric annuli with small radius ratios for the Reynolds number range $Re = 2 \times 10^4$–$2 \times 10^5$. Nouri *et al.* [5] and Escudier *et al.* [6] performed an LDV experiment in concentric annuli for a radius ratio $\alpha = 0.5$. They used non-Newtonian fluids to take into account realistic flow characteristics. Meanwhile, some experiments on annular channel flow involved heat transfer have been carried out. Heikal *et al.* [7] measured the velocity field in heated flow of air through an annular channel. Hasan *et al.* [8], Velidandla *et al.* [9] and Kang *et al.* [10] carried out experimental studies on the velocity and temperature fields in turbulent unheated and heated liquid flow through a vertical concentric annular channel. Those experiments reasonably predicted higher turbulence intensities near the inner wall than those near the outer wall, when the turbulence characteristics are scaled by bulk mean velocity. On the other hand, only have few computations been performed on turbulent flow in concentric annular channel. Hanjalic [11] studied the turbulence behaviour in annular ducts based on the Reynolds-averaged Navier–Stokes (RANS) with differential transport model. Malik and Pletcher [12] examined the performance of some turbulence models on the flow with heat transfer in ducts of annular cross-section. Zarate *et al.* [13] carried out the RANS of isothermal and heated turbulent upward flow in a vertical concentric annular channel with its inner wall heated. Azouz and Shirazi [14] evaluated several RANS models to predict the turbulent flow in concentric annuli and compared their results with the experimental data given by Nouri *et al.* [5]. Recently, Chung *et al.* [15] performed a direct numerical simulation on annular channel flows at low Reynolds number. To the best of our knowledge, however, little work has been performed for the investigation of turbulent concentric annular channel flow by use of large eddy simulation (LES) approach.

As well known, the LES technique provides an effective tool for the prediction of complex turbulent flows by computing only the large-scale components and modelling the subgrid-scale (SGS) motion. The accuracy of LES method depends significantly on the ability of SGS model to characterize the effect of the unresolved motion on the resolved scales. Prediction of classical algebraic model, proposed by Smagorinsky [16], has showed that this algebraic model is accurate only as long as the full inertial range is resolved, and even then the model coefficient has to be varied for different flows, which makes the universal application of this model questionable. A dynamic SGS model was proposed by Germano *et al.* [17] which overcome some shortcomings of the classical Smagorinsky model [16]. The dynamic model gained a remarkable success in the past decade and gave a new impetus to the development of

 

new strategies for LES. Although some work has shown the superior ability of this dynamic model, there remain some inherent limitations due to the nature of the algebraic model. Kim and Menon [18] proposed a localized one-equation dynamic subgrid model (LDM) where the similarity between the subgrid-scale stress tensor and the test-scale Leonard stress tensor is used to evaluate the model coefficient. The scale similarity invoked in the LDM is based on experimental measurement performed by Liu *et al.* [19] in high-Reynolds number turbulent flows. This feature allows the LDM to overcome some of the inherent shortcomings of the Germano-type dynamic models. The LDM model's capability of predicting correctly the turbulence features is tested based on calculations on wall bounded turbulent flows [20]. Pallares and Davidson [21] achieved to reveal the stabilization or destabilization effects of the Coriolis force on turbulent shear flow in a rotating square duct with the LDM model. So, it is a worthy attempt to use the LDM model to simulate turbulent annular channel flow. Thus, LES coupled with the LDM model is carried out in this study to investigate turbulent flow behaviour near the walls in a concentric annular channel.

This paper is organized as follows. The governing equations and the localized one-equation dynamic SGS model are described in the next section. In Section 3, numerical method and its validation are presented. In Section 4, calculated results including the mean velocity, turbulence intensities, eddy viscosity coefficient, budgets in the turbulent energy, and flow structures based on the velocity fluctuations are shown and discussed. Conclusions are summarized in Section 5.

## 2. GOVERNING EQUATIONS

### 2.1. Filtered Navier–Stokes equations

The governing equations are the three-dimensional resolved incompressible Navier–Stokes equations. To non-dimensionalize the governing equations, the gap width of the annular channel, $d = R_o - R_i$ with $R_o$ and $R_i$ being the outer and inner cylinder radius, respectively, and the averaged friction velocity $u_\tau$, which is described in the following subsection, are taken as the length and velocity scales. Then, the non-dimensional governing equations are given as

$$\frac{\partial \bar{u}_i}{\partial x_i} = 0 \tag{1}$$

$$\frac{\partial \bar{u}_i}{\partial t} + \frac{\partial}{\partial x_j}(\bar{u}_i \bar{u}_j) = -\frac{\partial \bar{p}}{\partial x_i} + \frac{1}{Re_\tau}\frac{\partial^2 \bar{u}_i}{\partial x_j \partial x_j} - \frac{\partial \tau_{ij}}{\partial x_j} \tag{2}$$

where $Re_\tau$ is the Reynolds number, defined as $Re_\tau = u_\tau d/\nu$ with $\nu$ being the kinematic viscosity of the fluid, $\bar{u}_i$ and $\bar{p}$ are the resolved velocity and pressure, respectively. $\tau_{ij}$ is the SGS stress tensor,

$$\tau_{ij} = \overline{u_i u_j} - \bar{u}_i \bar{u}_j \tag{3}$$

As shown in Figure 1, it is a natural choice to solve the Navier–Stokes equations in cylindrical co-ordinates. Verzicco and Orlandi [22] introduced new variables $q_r = r\bar{v}_r$, $q_\theta = r\bar{v}_\theta$, and $q_z = \bar{v}_z$ into the Navier–Stokes equations in the cylindrical co-ordinates, where $\bar{v}_r$, $\bar{v}_\theta$ and $\bar{v}_z$

 

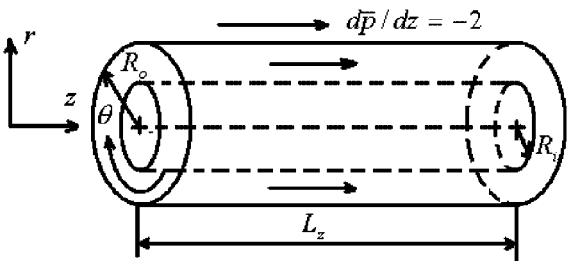


Figure 1. Sketch of a concentric annular channel.

represent the radial, azimuthal and axial resolved velocity components, respectively. The non-dimensional resolved incompressible Navier–Stokes equations in terms of the new variables can be written as

$$\frac{\partial q_r}{\partial r} + \frac{1}{r}\frac{\partial q_\theta}{\partial \theta} + r\frac{\partial q_z}{\partial z} = 0 \tag{4}$$

$$\begin{aligned}
&\frac{\partial q_r}{\partial t} + \frac{\partial}{\partial r}\left(\frac{q_r q_r}{r}\right) + \frac{\partial}{\partial \theta}\left(\frac{q_\theta q_r}{r^2}\right) + \frac{\partial (q_r q_z)}{\partial z} - \frac{q_\theta q_\theta}{r^2} \\
&\quad = -r\frac{\partial P}{\partial r} + \frac{1}{Re_\tau}\left[\frac{\partial}{\partial r}\left(\nu_T \frac{\partial q_r}{\partial r}\right) - \frac{1}{r}\frac{\partial (\nu_T q_r)}{\partial r} + \frac{1}{r^2}\frac{\partial}{\partial \theta}\left(\nu_T \frac{\partial q_r}{\partial \theta}\right) + \frac{\partial}{\partial z}\left(\nu_T \frac{\partial q_r}{\partial z}\right)\right] \\
&\qquad + \frac{1}{Re_\tau}\left\{\frac{\partial}{\partial r}\left(\nu_T \frac{\partial q_r}{\partial r}\right) - \frac{1}{r}\frac{\partial (\nu_T q_r)}{\partial r} + r\frac{\partial}{\partial \theta}\left[\nu_T \frac{\partial}{\partial r}\left(\frac{q_\theta}{r^2}\right)\right]\right. \\
&\qquad \left. + r\frac{\partial}{\partial z}\left(\nu_T \frac{\partial q_z}{\partial r}\right) - \frac{2\nu_T}{r^2}\frac{\partial q_\theta}{\partial \theta}\right\}
\end{aligned} \tag{5}$$

$$\begin{aligned}
&\frac{\partial q_\theta}{\partial t} + \frac{\partial (q_\theta q_r / r)}{\partial r} + \frac{q_\theta q_r}{r^2} + \frac{1}{r^2}\frac{\partial (q_\theta q_\theta)}{\partial \theta} + \frac{\partial (q_\theta q_z)}{\partial z} \\
&\quad = -\frac{\partial P}{\partial \theta} + \frac{1}{Re_\tau}\left\{\frac{\partial}{\partial r}\left[r\nu_T \frac{\partial}{\partial r}\left(\frac{q_\theta}{r}\right)\right] - \frac{q_\theta}{r^2}\frac{\partial (r\nu_T)}{\partial r} + \frac{1}{r^2}\frac{\partial}{\partial \theta}\left(\nu_T \frac{\partial q_\theta}{\partial \theta}\right) + \frac{\partial}{\partial z}\left(\nu_T \frac{\partial q_\theta}{\partial z}\right)\right\} \\
&\qquad + \frac{1}{Re_\tau}\left[\frac{1}{r}\frac{\partial}{\partial r}\left(\nu_T \frac{\partial q_r}{\partial \theta}\right) + \frac{1}{r^2}\frac{\partial}{\partial \theta}\left(\nu_T \frac{\partial q_\theta}{\partial \theta}\right) + \frac{\partial}{\partial z}\left(\nu_T \frac{\partial q_z}{\partial \theta}\right) + \frac{2}{r^2}\frac{\partial (\nu_T q_r)}{\partial \theta}\right]
\end{aligned} \tag{6}$$

$$\begin{aligned}
&\frac{\partial q_z}{\partial t} + \frac{1}{r}\frac{\partial (q_r q_z)}{\partial r} + \frac{1}{r^2}\frac{\partial (q_\theta q_z)}{\partial \theta} + \frac{\partial (q_z q_z)}{\partial z} \\
&\quad = -\frac{\partial P}{\partial z} + \frac{1}{Re_\tau}\left[\frac{1}{r}\frac{\partial}{\partial r}\left(r\nu_T \frac{\partial q_z}{\partial r}\right) + \frac{1}{r^2}\frac{\partial}{\partial \theta}\left(\nu_T \frac{\partial q_z}{\partial \theta}\right) + \frac{\partial}{\partial z}\left(\nu_T \frac{\partial q_z}{\partial z}\right)\right] \\
&\qquad + \frac{1}{Re_\tau}\left[\frac{1}{r}\frac{\partial}{\partial r}\left(\nu_T \frac{\partial q_r}{\partial z}\right) + \frac{1}{r^2}\frac{\partial}{\partial \theta}\left(\nu_T \frac{\partial q_\theta}{\partial z}\right) + \frac{\partial}{\partial z}\left(\nu_T \frac{\partial q_z}{\partial z}\right)\right]
\end{aligned} \tag{7}$$

 

where $\nu_T$ is total viscosity, defined as $\nu_T = 1 + \nu_\tau Re_\tau$, and $\nu_\tau$ is turbulence eddy viscosity determined by the localized dynamic SGS model described later. $P$ equals to the sum of filtered pressure $\bar{p}$ and $\tau_{kk}\delta_{ij}/3$.

In this study, fully developed turbulent flow in a concentric annular channel is assumed. Thus, periodic boundary conditions are employed in the axial and azimuthal directions. On the inner and outer cylinder walls, no-slip and no-penetration boundary conditions are used. The annular channel laminar flow is used as initial condition.

### 2.2. Axial force balance and scaling velocities

The annular channel flow is driven by an imposed non-dimensional mean pressure gradient in the axial direction, which is given as

$$\frac{\mathrm{d}\bar{p}}{\mathrm{d}z} = -2 \tag{8}$$

As the turbulent flow is assumed fully developed, flow features can be viewed as homogeneous in the axial ($z$) and azimuthal ($\theta$) directions, i.e. mean properties and turbulence statistics vary only in the radial ($r$) direction. The averaged friction velocity $u_\tau$ is defined as

$$u_\tau = \left( -\frac{\mathrm{d}}{2\rho} \frac{\mathrm{d}\bar{P}^*}{\mathrm{d}z^*} \right)^{1/2} \tag{9}$$

where $\rho$ is the fluid density and $\mathrm{d}\bar{P}^*/\mathrm{d}z^*$ identifies dimensional mean pressure gradient.

The mean flow velocities are only the function of $r$, $(U(r), V(r), W(r)) = (\langle \bar{v}_z \rangle, 0, 0)$, where $\langle\ \rangle$ denotes the time and spatial average. By integrating the averaged axial momentum equation in Equation (7) once with respect to $r$-direction, we can reach

$$-r\tau_{rz} + Re_\tau^{-1} r \frac{\mathrm{d}\langle \bar{v}_z \rangle}{\mathrm{d}r} = -(r^2 - R_\mathrm{i}^2) + \frac{R_\mathrm{i} u_\tau^{\mathrm{i}^2}}{u_\tau^2} \tag{10}$$

where $u_\tau^\mathrm{i}$ denotes the local friction velocity at the inner cylinder wall and is written as

$$u_\tau^{\mathrm{i}^2} = u_\tau^2 Re_\tau^{-1} \left. \frac{\mathrm{d}\langle \bar{v}_z \rangle}{\mathrm{d}r} \right|_{r=R_\mathrm{i}} \tag{11}$$

Correspondingly, $u_\tau^\mathrm{o}$ is the local friction velocity based on the wall shear stress at $r = R_\mathrm{o}$ and is read as

$$u_\tau^{\mathrm{o}^2} = u_\tau^2 Re_\tau^{-1} \left. \frac{\mathrm{d}\langle \bar{v}_z \rangle}{\mathrm{d}r} \right|_{r=R_\mathrm{o}} \tag{12}$$

Because the SGS stress $\tau_{ij}$ vanishes at the inner and outer walls, based on Equations (10) and (12), then the averaged friction velocity is expressed as

$$u_\tau^2 = \frac{R_\mathrm{i} u_\tau^{\mathrm{i}^2} + R_\mathrm{o} u_\tau^{\mathrm{o}^2}}{R_\mathrm{o} + R_\mathrm{i}} \tag{13}$$

Equation (13) indicates that the averaged friction velocity $u_\tau$ is the weighted average of the local friction velocities $u_\tau^\mathrm{i}$ and $u_\tau^\mathrm{o}$. This relationship can be used as a proof to examine whether calculated flow has reached the fully developed state.

 

### 2.3. Localized one-equation dynamic subgrid scale model

In the localized dynamic model (LDM), the grid scale is used to characterize the length scale, and the velocity scale is obtained by the SGS kinetic energy

$$k_{\mathrm{sgs}} = \tfrac{1}{2}(\overline{u_k u_k} - \bar{u}_k \bar{u}_k) \tag{14}$$

which is determined by solving the transport equation [23, 24]

$$\frac{\partial k_{\mathrm{sgs}}}{\partial t} + \frac{\partial k_{\mathrm{sgs}} \bar{u}_j}{\partial x_j} = -\tau_{ij} \frac{\partial \bar{u}_i}{\partial x_j} - \varepsilon_{\mathrm{sgs}} + \frac{1}{Re_\tau} \frac{\partial}{\partial x_j} \left( v_\tau \frac{\partial k_{\mathrm{sgs}}}{\partial x_j} \right) \tag{15}$$

Here, the three terms on the right-hand side represent production, dissipation and diffusion of $k_{\mathrm{sgs}}$, respectively. Also, $v_\tau$ denotes the eddy viscosity. By use of $k_{\mathrm{sgs}}$, the SGS stress tensor $\tau_{ij}$ is represented as [24, 25]

$$\tau_{ij} = -2 v_\tau \bar{s}_{ij} + \tfrac{2}{3} \delta_{ij} k_{\mathrm{sgs}} \tag{16}$$

$$v_\tau = C_\tau \bar{\Delta} k_{\mathrm{sgs}}^{1/2} \tag{17}$$

where $C_\tau$ is an adjustable coefficient to be determined dynamically, $\bar{\Delta}$ is the grid filter size and $\bar{s}_{ij}$ is the resolved-scale strain rate tensor

$$\bar{s}_{ij} = \tfrac{1}{2}(\bar{u}_{i,j} + \bar{u}_{j,i}) \tag{18}$$

Equation (15) is closed once the SGS dissipation rate $\varepsilon_{\mathrm{sgs}}$ is modelled. Based on scale analysis [24, 25], $\varepsilon_{\mathrm{sgs}}$ is usually modelled as

$$\varepsilon_{\mathrm{sgs}} = C_\varepsilon \frac{k_{\mathrm{sgs}}^{3/2}}{\bar{\Delta}} \tag{19}$$

where $C_\varepsilon$ is another coefficient which needs to be determined dynamically.

To obtain the localized dynamic SGS models [26], the procedure for computing the localized values of the model coefficients, $C_\tau$ and $C_\varepsilon$, is taken by introducing the definition of a test scale filter. Further, based on experimental measurement [19], similarity between the dynamic Leonard stresses, $L_{ij} = \hat{\bar{u}_i \bar{u}_j} - \hat{\bar{u}}_i \hat{\bar{u}}_j$, and the SGS stresses allows reasonable assumption of the similar formulation for tensors $\tau_{ij}$ and $L_{ij}$,

$$L_{ij} = -2 C_\tau \hat{\Delta} k_{\mathrm{test}}^{1/2} \hat{\bar{s}}_{ij} + \frac{1}{3} \delta_{ij} L_{kk} \tag{20}$$

where $\hat{\Delta}$ is the test filter size with $\hat{\Delta}/\bar{\Delta} = 2$ [17, 20], and $k_{\mathrm{test}}$ is the resolved kinetic energy at the test scale

$$k_{\mathrm{test}} = \tfrac{1}{2}(\hat{\bar{u}_k \bar{u}_k} - \hat{\bar{u}}_k \hat{\bar{u}}_k) \tag{21}$$

 

Here, note that $k_{\text{test}} = L_{kk}/2$. The energy is produced at the large scales by $-L_{ij}(\partial\hat{\bar{u}}_i/\partial x_j)$ and dissipated by

$$e = (\nu + \nu_\tau)\left(\widehat{\frac{\partial \bar{u}_i}{\partial x_j}\frac{\partial \bar{u}_i}{\partial x_j}} + \frac{\partial \hat{\bar{u}}_i}{\partial x_j}\frac{\partial \hat{\bar{u}}_i}{\partial x_j}\right) \tag{22}$$

The dynamic model coefficient $C_\tau$ in Equation (20) can be determined from the resolved quantities at the test filter level by applying the least-square method suggested by Lilly [27],

$$C_\tau = \frac{1}{2}\frac{L_{ij}\sigma_{ij}}{\sigma_{ij}\sigma_{ij}} \tag{23}$$

and

$$\sigma_{ij} = -\hat{\Delta}k_{\text{test}}^{1/2}\hat{\bar{s}}_{ij} \tag{24}$$

It should be noted that $\sigma_{ij}$ is determined completely by quantities at the test filter level.

Similarity between the dissipation rates $\varepsilon_{\text{sgs}}$ at the grid filter level and $e$ at the test filter level is also applied to obtain the dissipation model coefficient in this model. Thus

$$e = C_\varepsilon \frac{k_{\text{test}}^{3/2}}{\hat{\Delta}} \tag{25}$$

Then, $C_\varepsilon$ can be determined by Equation (22) and written as

$$C_\varepsilon = \hat{\Delta}(\nu + \nu_\tau)\left(\widehat{\frac{\partial \bar{u}_i}{\partial x_j}\frac{\partial \bar{u}_i}{\partial x_j}} - \frac{\partial \hat{\bar{u}}_i}{\partial x_j}\frac{\partial \hat{\bar{u}}_i}{\partial x_j}\right) \Big/ k_{\text{test}}^{3/2} \tag{26}$$

It can be verified that the LDM is a Galilean-invariant model and satisfies well the realizability conditions proposed by Schumann [28]. Furthermore, $k_{\text{sgs}}$ provides a more accurate estimation for the SGS velocity scale. The additional computational cost is primarily due to the inclusion of a transport equation for $k_{\text{sgs}}$, but the cost of this dynamic procedure is nearly the same as that of Germano-type dynamic model.

## 3. NUMERICAL METHODS AND VALIDATION

### *3.1. Numerical methods*

To perform LES calculation, a fractional method with three substeps is employed to solve Equations (4)–(7). Time advancement is carried out by the semi-implicit scheme mixing the second-order Crank–Nicolson scheme for the viscous terms and the third-order Runge–Kutta scheme for the convective terms. So, the algorithm is overall second-order accurate in time but the low-storage Runge–Kutta methods have the additional advantage that the minimum amount of computer run-time memory is realized. Spatial derivatives are discretized by the

 

Table I. Grid resolutions for different Reynolds numbers.

| $Re_\tau$ | 180 | 395 | 640 |
|---|---|---|---|
| $\Delta z^+$ | 28.13 | 61.72 | 75 |
| $\Delta r^+$ | $0.31 < \Delta r^+ < 6.48$ | $0.71 < \Delta r^+ < 14.22$ | $0.92 < \Delta r^+ < 15.36$ |
| $R_i \Delta\theta^+$ | 15.71 | 34.47 | 41.89 |
| $R_o \Delta\theta^+$ | 31.42 | 68.94 | 83.78 |

second-order central difference schemes. Detailed description of the numerical method has been given by Verzicco and Orlandi [22] and Rai and Moin [29].

Based on extensive tests with different grid numbers and time steps, the grid systems of $73 \times 65 \times 97$ and $97 \times 97 \times 128$ are adopted for the Reynolds number $Re_\tau = 180$, 395 and $Re_\tau = 640$, respectively. The corresponding grid resolutions are listed in Table I. Time step $\Delta t$ is chosen as 0.001. It has been verified that the present calculated results are independent of the grid number and time step. To achieve a fine grid resolution near the walls, a stretching transformation is employed to cluster the grids near the inner and outer wall in the radial direction and to resolve the viscous sublayer near the walls. The distance from the inner and outer wall of the annular channel in wall unit (i.e. $y_d^+$) is defined as

$$y_d^+ = \min[(r - R_i) Re_\tau/(R_o - R_i), (R_o - r) Re_\tau/(R_o - R_i)] \tag{27}$$

and the inner and outer cylinder radius are set to be $R_i = 1$ and $R_o = 2$, respectively. The annular channel length is chosen to be $L_z/d = 15$, which is a sufficient length to contain the largest coherent structure in the axial direction based on extensive validations, in which the computational domain size is chosen such that two-point correlations in the axial direction are negligibly small.

### 3.2. Validation

To examine the performance of the computational code, comparisons of our calculated results of turbulent pipe flows with experimental data [30] and DNS results [31] are taken. The averaged velocity and turbulent statistics are calculated for the pipe flows at the Reynolds number $Re_m = 4900$ and 24 600 based on the bulk mean velocity and pipe diameter, corresponding to $Re_\tau = 169$ and 690 approximately. Figure 2 shows the mean axial velocity profile, where $y^+ = Re_\tau(R - r)/R$ is the distance to the wall with $R$ being the pipe radius. It is noted that the present LES results are in good agreement with the experimental data [30] and DNS results [31].

Figures 3(a) and 3(b) are the turbulence intensities for $Re_m = 4900$ and 24 600, where $r_d = (R - r)/R$. At $Re_m = 4900$, the intensities in the axial and radial directions are compared fairly well with the experimental data [30] and DNS results [31]. At $Re_m = 24\,600$, the peak value of the axial intensity predicted by the LES is 2.87 approximately, while experimental data 2.68, at the same radial position. The radial intensity profile is reasonably consistent with the experiment data. Figure 3(c) shows the distribution of cross stress $\langle v_r' v_z' \rangle^+$. The LES result agrees well with the DNS result and experimental data. Moreover, we have compared other turbulent quantities with some previous DNS results (not shown here) and can confirm that our calculation code enables the LES results to be satisfactory.

 

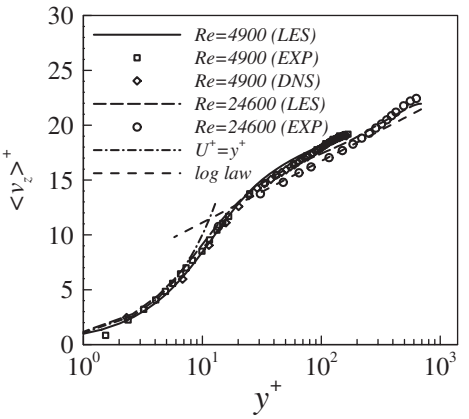


Figure 2. Profiles of mean axial velocity of pipe flows and their comparison with experimental data and DNS result normalized by the friction velocity.

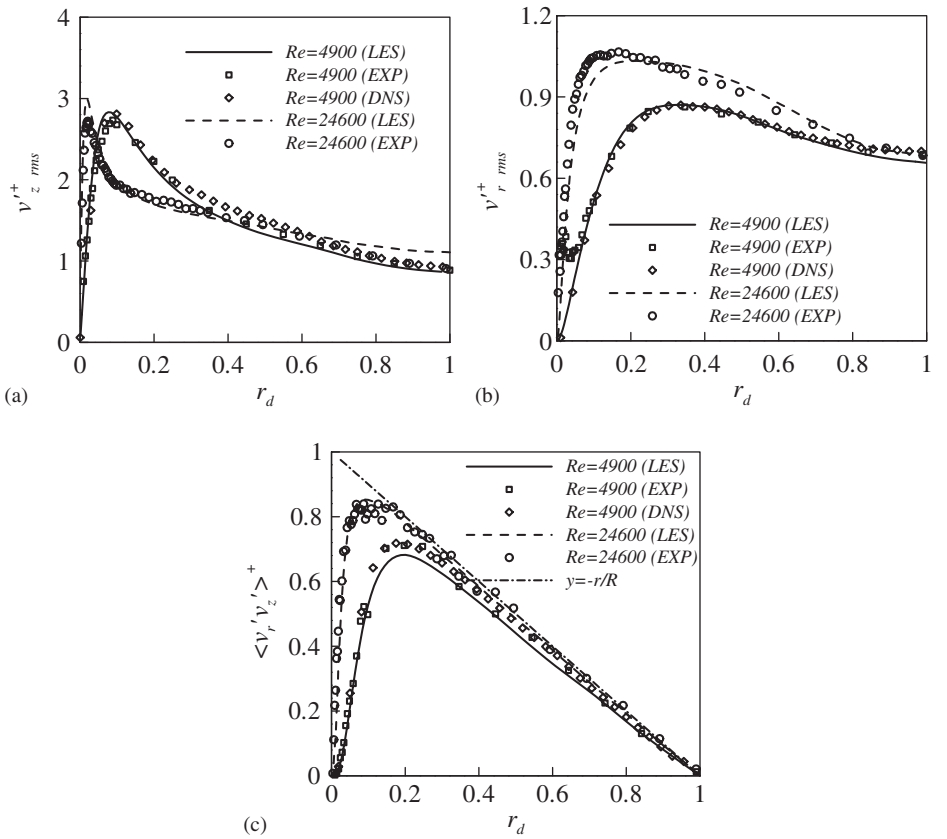


Figure 3. Profiles of the velocity fluctuations and Reynolds stress for pipe flows. (a) Axial velocity fluctuation; (b) radial velocity fluctuation; (c) $\langle v_r' v_z' \rangle^+$ Reynolds stress.

 

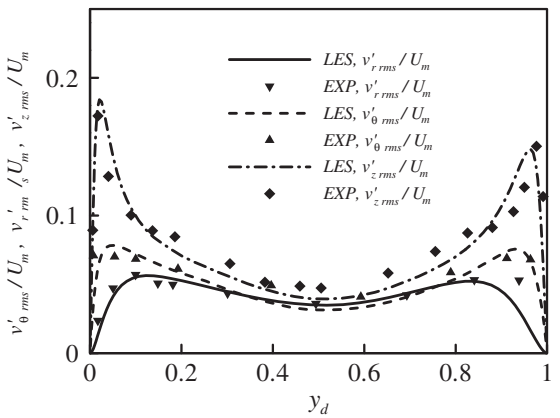


Figure 4. Turbulence intensities at $Re_\tau = 640$ and their comparison with the experiment data for turbulent annular channel flow.

Figure 4 shows the distributions of the turbulence intensities for turbulent concentric annular channel flow versus the distance $y_d$ from the annular inner wall at $Re_\tau = 640$ (corresponding to $Re_m = 15\,200$ approximately), where $y_d = (r - R_i)/(R_o - R_i)$. By comparing the present LES results with available experimental data at $Re_m = 13\,300$ [5], it is seen that our LES results are in good agreement with the experimental data although both the Reynolds numbers are somewhat different. Other turbulence statistics have been verified based on comparison between our calculated results and the experimental data [5]. Furthermore, the corresponding computational code used in this study has been validated and verified by our previous work [32–34]. Thus, it can be confirmed that our calculation is reliable for the prediction of statistical quantities of turbulent flow in a concentric annular channel.

## 4. RESULTS AND DISCUSSION

### *4.1. Mean velocity and friction velocity scaling*

The mean axial velocity profiles versus the distance $y_d$ from the inner annular cylinder are plotted in Figure 5. As the Reynolds number increases, turbulent viscous layers near both the walls become thinner, while the velocity distribution approaches to a more blunt shape profile in the core region of the annular channel. The position of the maximum mean axial velocity varies with the Reynolds number, which is the main feature of asymmetric turbulent flow and consistent with Rehme's experiment [4]. If re-drawn the mean velocity profiles in logarithmic scale, it is found that there exists a buffer layer followed by a logarithmic region near both the walls.

The friction velocities at the inner and outer walls of the annular channel can be computed based on the velocity distributions in Figure 5. To ensure the axial force balance and to confirm that the turbulent flow has reached a fully developed statistic state in terms of Equation (13), the values of local friction velocities at the inner and outer wall and the ratio of the right- and left-hand sides of Equation (13) are listed in Table II. As expected, the friction

 

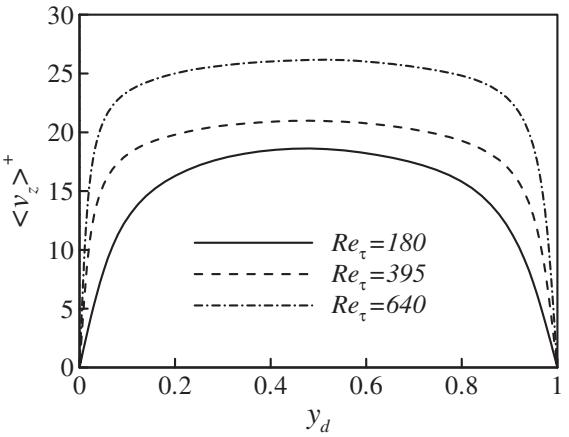


Figure 5. Profiles of mean axial velocity at different Reynolds numbers.

Table II. Local friction velocities for different Reynolds numbers.

| $Re_\tau$ | $\frac{u_\tau^{\mathrm{i}}}{u_\tau}$ | $\frac{u_\tau^{\mathrm{o}}}{u_\tau}$ | $\frac{u_\tau^{\mathrm{i}2} R_{\mathrm{i}} + u_\tau^{\mathrm{o}2} R_{\mathrm{o}}}{R_{\mathrm{i}} + R_{\mathrm{o}}} \Big/ u_\tau^2$ |
|---|---|---|---|
| 180 | 1.072 | 0.968 | 1.008 |
| 395 | 1.142 | 0.917 | 0.995 |
| 640 | 1.171 | 0.905 | 1.003 |

velocity at the inner wall is higher than that at the outer wall for the same Reynolds number. Generally, the higher friction velocity results in stronger shear stress at the wall, which thus causes higher turbulence level in the inner wall region. Meanwhile, based on the ratio of the right- and left-hand sides of Equation (13) approaching to unity, as listed in Table II, it means that fully developed turbulent flows have been reached in our calculations for those Reynolds numbers. This behaviour is consistent with the experimental data [5, 9, 10] and DNS result [15].

### *4.2. Turbulence intensities and Reynolds stresses*

Figure 6 shows the profiles of the axial turbulence intensity, i.e. the root-mean-square (rms) value of velocity fluctuation, scaled by the averaged friction velocity $u_\tau$ defined in Equation (13). The peak values of the axial turbulence intensity near the inner wall in Figure 6(a) are higher than those near the outer wall in Figure 6(b) for the same Reynolds number. In this problem, although higher level of the distribution of the axial rms velocity appears near the inner wall, the inner wall may totally supply relatively less turbulent kinetic energy than the outer wall since the surface area of the inner wall is smaller than that of the outer wall.

As shown in Figure 7, if re-scaled by local friction velocities $u_\tau^{\mathrm{i}}$ and $u_\tau^{\mathrm{o}}$ near the inner and outer wall, respectively, the peak value of the axial turbulence intensity near the inner wall

 

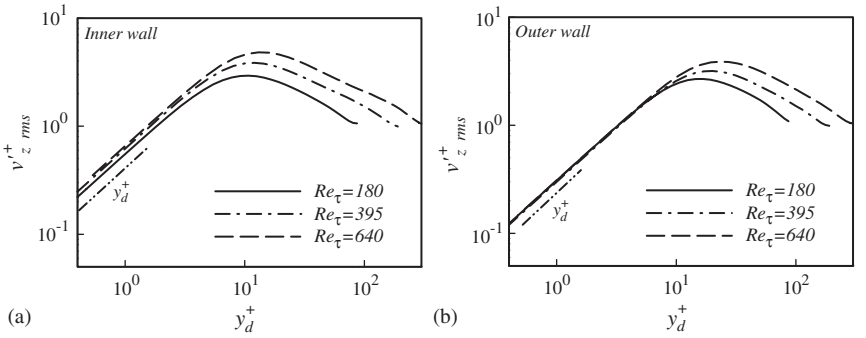


Figure 6. Profiles of the axial turbulence intensity for different Reynolds numbers: (a) inner wall; (b) outer wall.

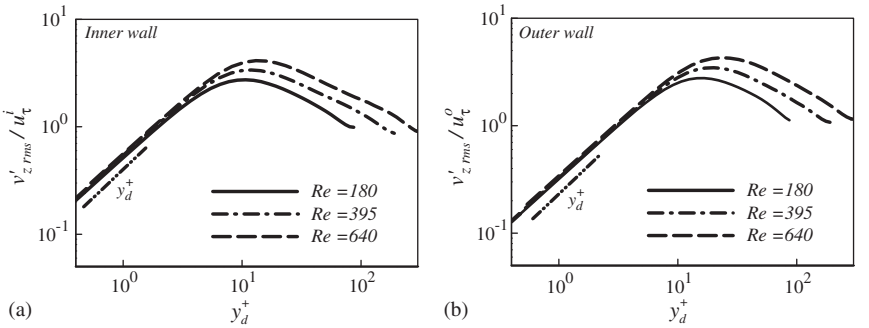


Figure 7. Profiles of the axial turbulence intensity scaled by local friction velocities: (a) inner wall; (b) outer wall.

in Figure 7(a) is lower than that near the outer wall in Figure 7(b) for the same Reynolds number. This behaviour is consistent with the DNS results [15], where statistical quantities were scaled by the local friction velocities $u_\tau^{\mathrm{i}}$ and $u_\tau^{\mathrm{o}}$ near the inner and outer wall, respectively. In extensive experiments [4, 5, 9, 10], however, turbulence statistical quantities for the annular channel turbulent flow were usually normalized by a uniform velocity scale, e.g. bulk mean velocity. According to the experimental data [4, 5, 9, 10], it is noted that, similar to Figure 6, the peak values of turbulence intensities near the inner wall are higher than those near the outer wall. This behaviour can be reasonably explained based on the local friction velocities $u_\tau^{\mathrm{i}}$ and $u_\tau^{\mathrm{o}}$ listed in Table II with $u_\tau^{\mathrm{i}}$ being higher than $u_\tau^{\mathrm{o}}$. If using different velocity scales to normalize statistical quantities, it may be somewhat to result in misunderstanding. Thus, following the treatment of those experiments, we employ the averaged friction velocity $u_\tau$ as a uniform velocity scale to normalize the statistical quantities near the inner and outer wall of the annular channel.

To reveal the near wall behaviour of the velocity fluctuations, based on the analysis of turbulent pipe flow [30] and turbulent channel flow [35], the velocity fluctuations, i.e. $v_z'$, $v_r'$ and $v_\theta'$, can be expanded into power series of $y_{\mathrm{d}}^+$ in the vicinity of the inner and outer wall

 

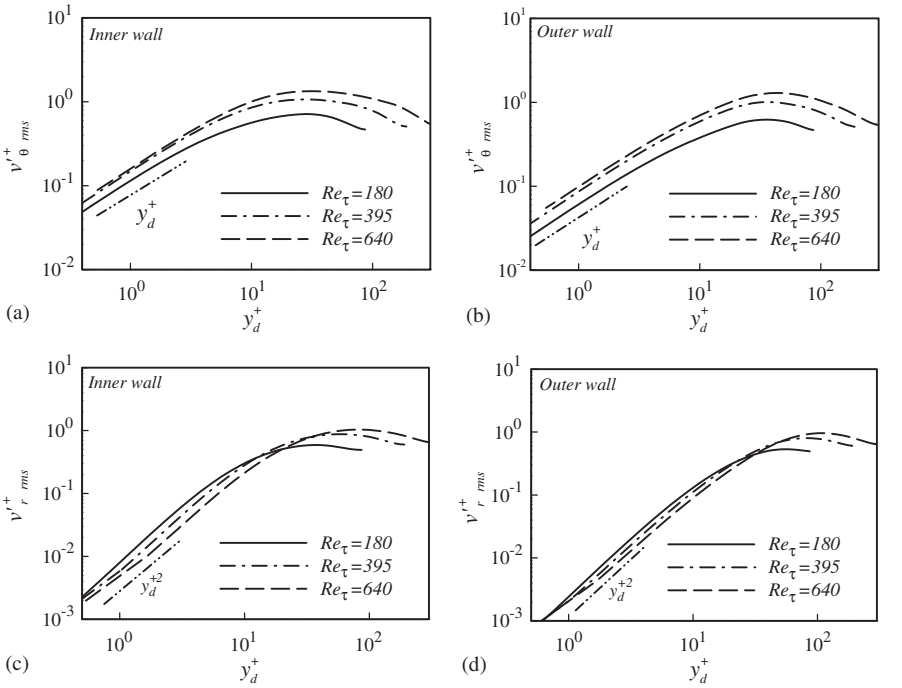


Figure 8. Profiles of the azimuthal and radial turbulence intensities: (a) azimuthal intensity near the inner wall; (b) azimuthal intensity near the outer wall; (c) radial intensity near the inner wall; (d) radial intensity near the outer wall.

of the annular channel,

$$v'_z = a_1 y_{\mathrm{d}}^+ + a_2 y_{\mathrm{d}}^{+2} + a_3 y_{\mathrm{d}}^{+3} + \cdots \tag{28a}$$

$$v'_r = b_2 y_{\mathrm{d}}^{+2} + b_3 y_{\mathrm{d}}^{+3} + \cdots \tag{28b}$$

$$v'_\theta = c_1 y_{\mathrm{d}}^+ + c_2 y_{\mathrm{d}}^{+2} + c_3 y_{\mathrm{d}}^{+3} + \cdots \tag{28c}$$

Then, curve of the linear law with the distance from the walls (i.e. $y_{\mathrm{d}}^+$) is plotted in Figures 6 and 7 with logarithmic scales to illustrate the first term in (28a). As expected, the axial turbulence intensity agrees well with the leading term behaviour in (28a) near the inner and outer wall, respectively.

The radial and azimuthal turbulence intensities are shown in Figure 8 and are similar to the features of turbulent plate channel flow weakly rotating along its spanwise direction [36]. This fact is due to the analogy of the transverse curvature effect and the centrifugal behaviour due to extra rotation [37]. The transverse curvature effect destabilizes the azimuthal velocity fluctuation near the inner wall and enhances the kinetic energy transfer from the axial velocity component to the azimuthal fluctuation by sweep events, while the transverse curvature effect acts an opposite effect on the flow near the outer wall. Thus, the azimuthal turbulence intensity reaches a higher level near the inner wall in Figure 8(a), compared to that near the outer

 

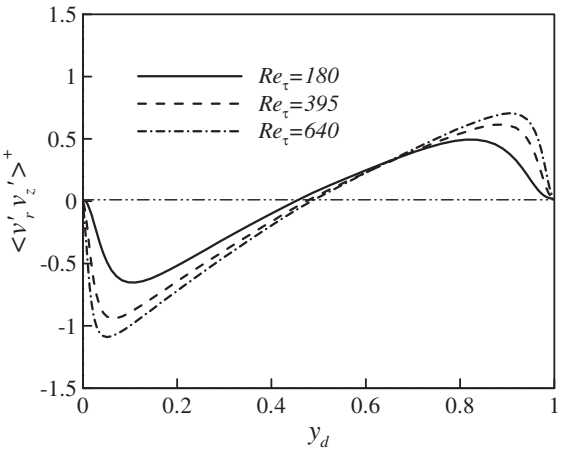


Figure 9. Profiles of the radial-axial Reynolds stress for different Reynolds numbers.

wall in Figure 8(b). With the increase of the Reynolds number, the boundary layers of the annular channel become thinner, and the positions of the peak values of the azimuthal intensity shifts closer to both the walls. The profiles of the radial turbulence intensity are shown in Figures 8(c) and 8(d). As the Reynolds number increases, the radial turbulence fluctuation gets more energy by the redistribution process of turbulent kinetic energy due to the stronger mean shear stress in the wall regions. Thus, higher level distribution of the radial turbulence intensity is formed for larger Reynolds number. Meanwhile, both curves of the linear and square laws with the distance from the walls (i.e. $y_{\mathrm{d}}^{+}$) are drawn in Figure 8 with logarithmic scales to exhibit the first terms in (28b) and (28c). It is noted that the radial and azimuthal turbulence intensities agree well with the leading terms behaviour in (28b) and (28c) near the walls, respectively.

Figure 9 is the distribution of Reynolds stress $\langle v_r' v_z' \rangle$ for $Re_\tau = 180$, 395 and 640. It is noted that $\langle v_r' v_z' \rangle$ is nearly linear in the core region of the annular channel and the slope of $\langle v_r' v_z' \rangle$ increases with the increase of the Reynolds number. The zero Reynolds stress positions are $y_{\mathrm{d}} = 0.455$, 0.475 and 0.488 approximately for $Re_\tau = 180$, 395 and 640, respectively. The asymmetric feature is also the reason that most turbulence models failed to simulate the turbulent flows in the annular channel in RANS prediction.

### *4.3. Quantities from LDM model*

Figure 10 shows the averaged turbulent eddy viscosity calculated by Equation (17), where $\langle\ \rangle_p$ denotes spatial average in the $(\theta, z)$-plane. The turbulent eddy viscosity varies smoothly cross the annular channel at $Re_\tau = 180$. However, as the Reynolds number increases to $Re_\tau = 395$ and 640, the averaged turbulent eddy viscosity alters significantly in the near wall regions and forms two peaks at $y_{\mathrm{d}} = 0.2$ and 0.8 approximately. The profiles of $\langle v_\tau \rangle_p$ reach the minimum in the core region of the annular channel.

Figure 11 shows the distributions of the SGS kinetic energy $k_{\mathrm{sgs}}$ defined in Equation (14), which is obtained by solving the transport equation of $k_{\mathrm{sgs}}$. As mentioned above, the turbulent intensity near the inner wall is larger than that near the outer wall due to the transverse

 

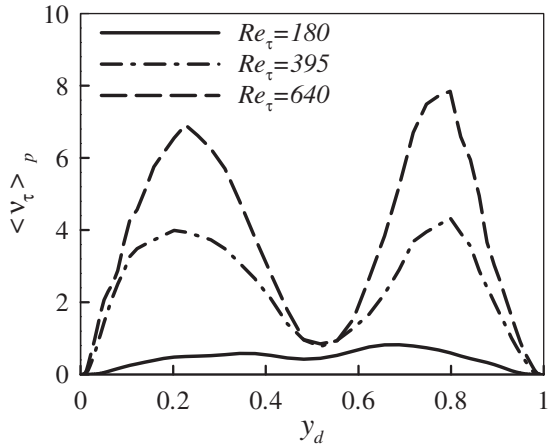


Figure 10. Profiles of mean turbulent eddy viscosity.

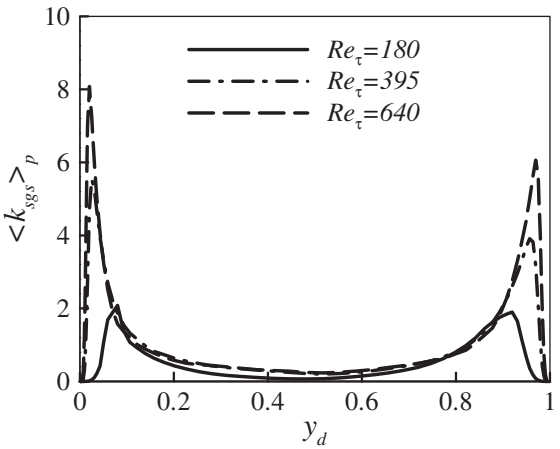


Figure 11. Profiles of mean subgrid scale kinetic energy.

curvature effect. Thus, a higher value of the SGS energy is expected in the vicinity of the inner wall. In the core region of the annular channel, the profiles of the SGS kinetic energy almost approach to the similar distribution for different Reynolds numbers. It is due to the fact that the velocity fluctuations in the core region of the annular channel, in particular for the axial velocity fluctuation, vary small as the Reynolds number increases, as shown in Figures 6 and 8.

The profiles of the SGS dissipation $\varepsilon_{sgs}$ are plotted in Figure 12 to exhibit the influence of the transverse curvature. $\varepsilon_{sgs}$ varies evidently in the wall regions with the increase of the Reynolds number. Similar to the distribution of $k_{sgs}$ in Figure 11, $\varepsilon_{sgs}$ reaches a higher peak

 

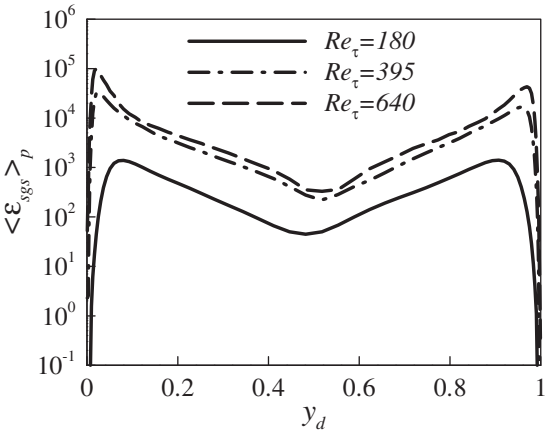


Figure 12. Profiles of mean subgrid scale dissipation rate.

value near the inner wall with respect to that near the outer wall. In the core region of the annular channel, the SGS dissipation rate decays rapidly.

### *4.4. Resolved Reynolds stress budgets*

The resolved Reynolds stress budgets are helpful to understand the transverse curvature effect on dynamical characteristics of turbulence based on production rate, redistribution and dissipation rate of turbulent kinetic energy. In this asymmetric turbulent flow, the axial Reynolds stress contributes mainly to the turbulent kinetic energy, and the azimuthal turbulence fluctuation behaves differently from that of plate channel flow in the wall regions due to the transverse curvature effect. So, it is needed to investigate the turbulence production and dissipation rate near the wall regions based on the budgets of the axial and azimuthal Reynolds stresses.

The turbulent energy transport equations of the annular channel flow can be obtained from the resolved incompressible Navier–Stokes equations in cylindrical co-ordinates. As the turbulent annular flow is considered to be fully developed and homogeneous in the azimuthal and axial directions, the only non-zero mean velocity is the axial velocity component, and all derivatives of the mean quantities in the axial and azimuthal directions disappear. The remaining terms of the Reynolds stress budgets under consideration are, according to the definition of Moin and Kim [38], production rate (PRD), velocity pressure-gradient term (VPG), diffusion rate (DFS), and dissipation rate (DSP), which are described as follows:

(1) Principal budget terms in $\langle v_\theta'^2 \rangle$-transport equation:

PRD (production rate): $-2\langle v_r' v_\theta' \rangle \dfrac{1}{r} \dfrac{\partial (r\langle \bar{v}_\theta \rangle)}{\partial r}$;

VPG (velocity pressure-gradient term): $-2\left\langle v_\theta' \dfrac{1}{r} \dfrac{\partial p'}{\partial \theta} \right\rangle$;

 

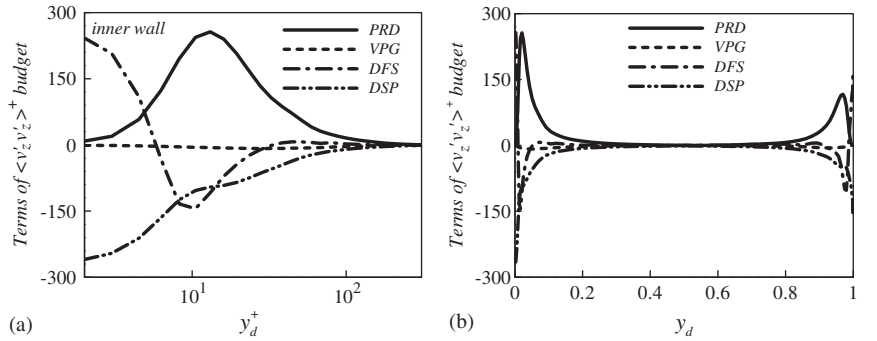


Figure 13. Terms in budget of $\langle v_z' v_z' \rangle$ at $Re_\tau = 640$: (a) near the inner wall; (b) over the channel.

DSF (diffusion rate): $\dfrac{1}{Re_\tau}\left\langle \dfrac{1}{r}\dfrac{\partial}{\partial r}\left[r^3 \nu_T \dfrac{\partial}{\partial r}\left(\dfrac{v_\theta'^2}{r^2}\right)\right]\right\rangle$;

DSP (dissipation rate): $-\dfrac{2}{Re_\tau}\left\{r^2\left\langle \nu_T\left[\dfrac{\partial}{\partial r}\left(\dfrac{v_\theta'}{r}\right)\right]^2\right\rangle + \dfrac{1}{r^2}\left\langle \nu_T\left(\dfrac{\partial v_\theta'}{\partial \theta}\right)^2\right\rangle + \left\langle \nu_T\left(\dfrac{\partial v_\theta'}{\partial z}\right)^2\right\rangle\right\}$

(2) Principal budget terms in $\langle v_z'^2 \rangle$-transport equation:

PRD (production rate): $-2\langle v_r' v_z' \rangle \dfrac{\partial \langle \bar{v}_z \rangle}{\partial r}$;

VPG (velocity pressure-gradient term): $-2\left\langle v_z' \dfrac{\partial p'}{\partial z}\right\rangle$;

DFS (diffusion rate): $\dfrac{1}{Re_\tau}\left\langle \dfrac{1}{r}\dfrac{\partial}{\partial r}\left(r\nu_T \dfrac{\partial v_z'^2}{\partial r}\right)\right\rangle$;

DSP (dissipation rate): $-\dfrac{2}{Re_\tau}\left[\left\langle \nu_T\left(\dfrac{\partial v_z'}{\partial r}\right)^2\right\rangle + \dfrac{1}{r^2}\left\langle \nu_T\left(\dfrac{\partial v_z'}{\partial \theta}\right)^2\right\rangle + \left\langle \nu_T\left(\dfrac{\partial v_z'}{\partial z}\right)^2\right\rangle\right]$

(3) Principal budget terms in $\langle v_r' v_z' \rangle$-transport equation:

PRD (production rate): $-\langle v_r' v_r' \rangle \dfrac{\partial \langle \bar{v}_z \rangle}{\partial r}$;

VPG (velocity pressure-gradient term): $-\left(\left\langle v_z' \dfrac{\partial p'}{\partial r}\right\rangle + \left\langle v_r' \dfrac{\partial p'}{\partial z}\right\rangle\right)$;

DFS (diffusion rate): $\dfrac{1}{Re_\tau}\left\langle \dfrac{1}{r}\dfrac{\partial}{\partial r}\left[r\nu_T \dfrac{\partial (v_r' v_z')}{\partial r}\right]\right\rangle$;

DSP (dissipation rate): $-\dfrac{2}{Re_\tau}\left[\left\langle \nu_T \dfrac{\partial v_r'}{\partial r}\dfrac{\partial v_z'}{\partial r}\right\rangle + \dfrac{1}{r^2}\left\langle \nu_T \dfrac{\partial v_r'}{\partial \theta}\dfrac{\partial v_z'}{\partial \theta}\right\rangle + \left\langle \nu_T \dfrac{\partial v_r'}{\partial z}\dfrac{\partial v_z'}{\partial z}\right\rangle\right]$

Figure 13 shows the budget terms of the axial Reynolds stress $\langle v_z' v_z' \rangle$ at $Re_\tau = 640$. In the near wall region, as shown in Figure 13(a), the balance of $\langle v_z' v_z' \rangle$ budget is mainly due to the interaction between DFS and DSP terms in the viscous sublayer ($y_d^+ < 10$). While in the region $10 < y_d^+ < 80$, the magnitude of PRD is as large as those of DFS and DSP. The maximum

 

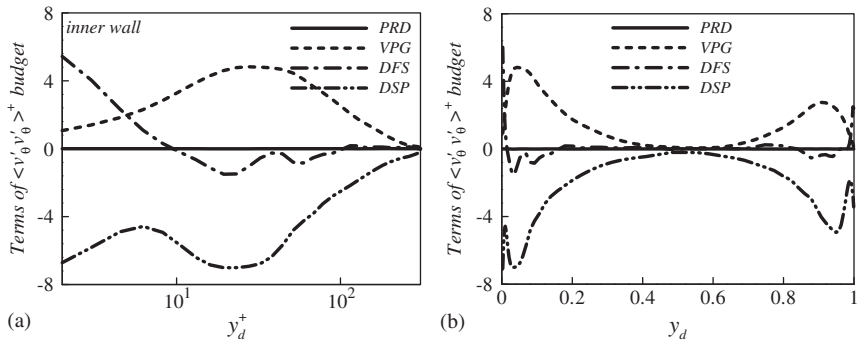


Figure 14. Terms in budget of $\langle v'_\theta v'_\theta \rangle$ at $Re_\tau = 640$: (a) near the inner wall; (b) over the channel.

of PRD of $\langle v'_z v'_z \rangle$ appears at $y_d^+ = 16$ approximately. The VPG term is much smaller than other three terms over the annular channel, but it mainly contributes to the turbulent energy redistribution [38], because it drains the turbulent energy from the axial turbulence fluctuation to the azimuthal and radial components. In the region far from the walls, all the four terms decay rapidly. Due to the transverse curvature effect, as shown in Figure 13(b), a higher level of PRD in $\langle v'_z v'_z \rangle$ appears in the inner wall region, which indicates that more active dynamic process results in generating stronger axial turbulence fluctuation near the inner wall. The DFS term plays an important role to $\langle v'_z v'_z \rangle$ budget in the inner wall region compared to that in the outer wall region.

The budget terms of the azimuthal Reynolds stress $\langle v'_\theta v'_\theta \rangle$ at $Re_\tau = 640$ are plotted in Figure 14. Because the azimuthal mean velocity vanishes, the PRD of $\langle v'_\theta v'_\theta \rangle$ turns to be zero over the annular channel. By comparing with the budget terms of $\langle v'_z v'_z \rangle$, the DSP, DFS and VPG terms are smaller. It can be explained as that the azimuthal turbulence fluctuation is generated by the sweep and ejection events inhabiting high- and low-speed elongated streaky coherent structure near the walls, while the axial turbulence fluctuation is generated by the strong shear process of the mean axial flow. In this asymmetric turbulent flow, the transverse curvature effect enhances the azimuthal fluctuation in the vicinity of the inner wall. The budget terms of $\langle v'_\theta v'_\theta \rangle$, i.e. the DSP, DFS and VPG terms, are mainly contributed to the budget balance near the inner wall in Figure 14(a). It can be seen that the VPG term acts as a source term to the azimuthal normal Reynolds stress. This behaviour is similar to turbulent plate channel flow. The DSP is mainly balanced by the VPG in the region of $10 < y_d^+ < 150$, while by the DFS in the inner wall region.

Figure 15 shows the profiles of the budget terms of cross Reynolds stress $\langle v'_r v'_z \rangle$ at $Re_\tau = 640$. According to its definition of PRD, $\langle v'_r v'_z \rangle$ is directly relevant to the mean shear in the annular channel. Due to the influence of the transverse curvature, as shown in Figure 15, a higher value of PRD appears near the inner wall. It is shown that the balance of $\langle v'_r v'_z \rangle$ budget is mainly due to the interaction between the PRD and VPG terms. Only in the region $y_d^+ < 8$, the contribution of the DFS and DSP terms cannot be neglected in the transport equation of $\langle v'_r v'_z \rangle$.

 

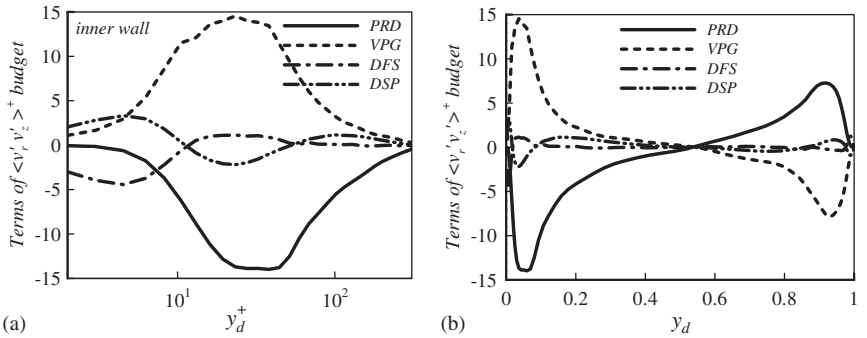


Figure 15. Terms in budget of $\langle v_r' v_z' \rangle$ at $Re_\tau = 640$: (a) near the inner wall; (b) over the channel.

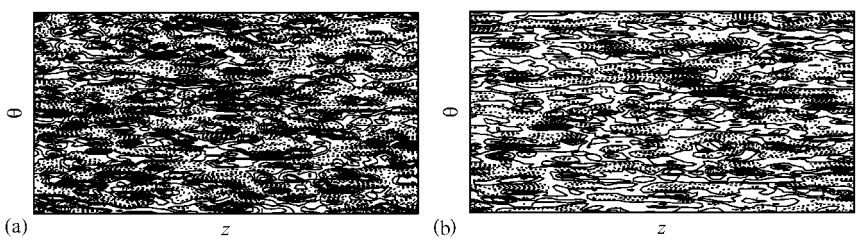


Figure 16. Contours of instantaneous azimuthal velocity fluctuation $v_\theta'$ in the $(\theta, z)$-plane near the walls at $Re_\tau = 640$ with the contour increment $\Delta v_\theta' = 0.2$: (a) $y_d = 0.02$; (b) $y_d = 0.98$.

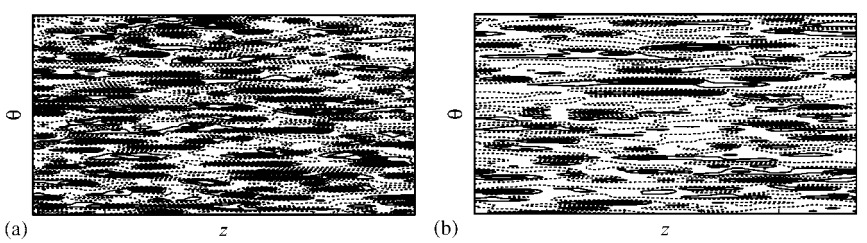


Figure 17. Contours of instantaneous axial velocity fluctuation $v_z'$ in the $(\theta, z)$-plane near the walls at $Re_\tau = 640$ with the contour increment $\Delta v_z' = 1.8$: (a) $y_d = 0.02$; (b) $y_d = 0.98$.

### 4.5. Flow structures

To reveal the influence of the transverse curvature on turbulence structures in the near wall regions, Figures 16 and 17 show the contours of instantaneous azimuthal and axial velocity fluctuations, i.e. $v_\theta'$ and $v_z'$, in the $(\theta, z)$-plane at $y_d = 0.02$ (i.e. near the inner wall) and 0.98 (i.e. near the outer wall) at $Re_\tau = 640$. As shown obviously in Figure 16, the azimuthal fluctuation $v_\theta'$ is more active near the inner wall in Figure 16(a). The higher value $v_\theta'$ near

 

the inner wall is associated with a large number of intensive sweep and ejection events and attributed to the transverse curvature effect, which enhances the azimuthal turbulence fluctuation near the inner wall. By comparing with the patterns of $v_z'$ in Figure 17, it is seen that the axially elongated high- and low-speed streaks in the inner wall region are more active in Figure 17(a). The flow structures are well consistent with statistical results shown in Figures 6 and 8.

## 5. CONCLUDING REMARKS

Large eddy simulation coupled with one-equation localized dynamic subgrid-scale model is performed to deal with turbulent annular channel flows at $Re_\tau = 180$, 395 and 640. The decisive validation of the present approach has been achieved by comparing our calculated results with some available computational and experimental results. Based on our calculated results, it is noted that there exists a buffer layer followed by a logarithmic region near the inner and outer walls from the mean axial velocity profiles. The profile of turbulence intensity is asymmetric over the annular channel, if normalized by a uniform averaged friction velocity $u_\tau$, with higher peak value near the inner wall and lower peak value near the outer wall for the parameters considered in this study. Meanwhile, if re-scaled by local friction velocities $u_\tau^{\mathrm{i}}$ and $u_\tau^{\mathrm{o}}$ near the inner and outer wall, respectively, it is interesting to find that the turbulence intensity near the outer wall is higher than that near the inner wall. These behaviours are reasonably consistent with available experimental data and DNS results and can be explained as different local friction velocities near the inner and outer walls. It is evident that the non-coincidence of the positions of the zero Reynolds stress and maximum velocity results from the asymmetry of the annular channel flow in which the diffusion of turbulent energy plays an important role. To elucidate the turbulent characteristics near the inner and outer wall, the turbulent eddy viscosity, SGS kinetic energy, and SGS dissipation rate are analysed. Further, the resolved Reynolds stress budgets are calculated to deal with the transverse curvature effect on dynamical characteristics of turbulence based on production rate, redistribution and dissipation rate of turbulent kinetic energy. Those budget terms indicate the enhancement of turbulence production rate and dissipation rate near the inner wall due to the transverse curvature effect. Flow structures based on the velocity fluctuations also verify that the sweep and ejection events near the inner wall are more active compared to those near the outer wall.

ACKNOWLEDGEMENTS

The authors are grateful to Dr. J. M. J. Den Toonder and Dr. F. T. M. Nieuwstadt for their providing the original experimental data cited in this paper. This work was supported by the National Natural Science Foundation of China (No.10302028, 10125210), the Programme of Hundred Talents of the Chinese Academy of Sciences (CAS), and Specialized Research Fund for the Doctoral Program of Higher Education (No. 20020358013).

REFERENCES

1. Brighton JA. The structure of fully-developed turbulence flow in annuli. *Ph.D. Thesis*, Purdue University, 1963.
2. Brighton JA, Jones JB. Fully-developed turbulent flow in annuli. *Journal of Basic Engineering*, *D* 1964; **86**: 835–844.

 

3. Lawn CJ, Elliott CJ. Fully-developed turbulent flow through concentric annuli. *C. E. G. B. Report RD/B/N* 1878, 1971.
4. Rehme K. Turbulence measurements in smooth concentric annuli with small radius ratios. *Journal of Fluid Mechanics* 1975; **72**:189–206.
5. Nouri JM, Umur H, Whitelaw JH. Flow of Newtonian and non-Newtonian fluids in concentric and eccentric annuli. *Journal of Fluid Mechanics* 1993; **253**:617–641.
6. Escudier MP, Gouldson IW, Jones DM. Flow of shear-thinning fluids in a concentric annulus. *Experiments in Fluids* 1995; **18**:225–238.
7. Heikal MRF, Walklate PJ, Hatton AP. The effect of free stream turbulence level on the flow and heat transfer in the entrance region of an annulus. *International Journal of Heat and Mass Transfer* 1976; **20**:763–771.
8. Hasan A, Roy RP, Kalra SP. Velocity and temperature fields in turbulent liquid flow through a vertical concentric annular channel. *International Journal of Heat and Mass Transfer* 1992; **35**:1455–1467.
9. Velidandla V, Putta S, Roy RP. Turbulent velocity field in isothermal and heated liquid flow through a vertical annular channel. *International Journal of Heat and Mass Transfer* 1996; **39**:3333–3346.
10. Kang S, Patil B, Zarate JA, Roy RP. Isothermal and heated turbulent upflow in a vertical annular channel—Part I. Experimental measurements. *International Journal of Heat and Mass Transfer* 2001; **44**:1171–1184.
11. Hanjalic K. Prediction of turbulent flow in annular ducts with differential transport model of turbulence. *Warme Stoffubertragung* 1974; **7**:72–78.
12. Malik MJ, Pletcher RH. A study of some turbulence models for flow and heat transfer in ducts of annular cross-section. *ASME Journal of Heat Transfer* 1981; **103**:146–152.
13. Zarate JA, Roy RP, Laporta A. Isothermal and heated turbulent upflow in a vertical annular channel—Part II. Numerical simulations. *International Journal of Heat and Mass Transfer* 2001; **44**:1185–1199.
14. Azouz I, Shirazi SA. Evaluation of several turbulence models for turbulent flow in concentric and eccentric annuli. *ASME Journal of Energy Resources Technology* 1998; **120**:268–275.
15. Chung SY, Rhee GH, Sung HJ. Direct numerical simulation of turbulent concentric annular pipe flow Part 1: Flow field. *International Journal of Heat and Fluid Flow* 2002; **23**:426–440.
16. Smagorinsky J. General circulation experiments with the primitive equations. *Monthly Weather Review* 1963; **91**:99–112.
17. Germano M, Piomelli U, Moin P, Cabot WH. A dynamic subgrid-scale eddy viscosity model. *Physics of Fluids* 1991; **3**:1760–1765.
18. Kim WW, Menon S. Application of the localized dynamic subgrid-scale model to turbulent wall-bounded flows. *AIAA*-97-0210, Reno, 1997.
19. Liu S, Meneveau C, Katz J. On the properties of similarity subgrid-scale models as deduced from measurements in a turbulent jet. *Journal of Fluid Mechanics* 1994; **275**:83–119.
20. Kim WW, Menon S. An unsteady incompressible Navier–Stokes solver for large eddy simulation of turbulent flows. *International Journal for Numerical Methods in Fluids* 1999; **31**:983–1017.
21. Pallares J, Davidson L. Large-eddy simulation of turbulent flow in a rotating square duct. *Physics of Fluids* 2000; **12**:2878–2893.
22. Verzicoo R, Orlandi P. A finite-difference scheme for three-dimensional incompressible flows in cylindrical coordinates. *Journal of Computational Physics* 1996; **123**:402–413.
23. Menon S, Yeuang PK, Kim WW. Effect of subgrid models on the computed interscale energy transfer in isotropic turbulence. *Computers & Fluids* 1996; **25**:165–180.
24. Schumann U. Subgrid scale model for finite difference simulations of turbulent flows in plane channels and annuli. *Journal of Computative Physics* 1975; **18**:376–404.
25. Yoshizawa A, Horiuti K. A statistically-derived subgrid-scale kinetic energy model for the large eddy simulation of turbulent flows. *Journal of the Physical Society of Japan* 1985; **54**:2834–2839.
26. Piomelli U. High Reynolds number calculations using the dynamic subgrid-scale stress model. *Physics of Fluids* 1993; **5**:1484–1490.
27. Lilly DK. A proposed modification of the Germano subgrid-scale closure method. *Physics of Fluids* 1992; **4**: 633–635.
28. Schumann U. Realizability of Reynolds-stress turbulence models. *Physics of Fluids* 1976; **20**:721–725.
29. Rai MM, Moin P. Direct simulation of turbulent flow using finite-difference schemes. *Journal of Computational Physics* 1991; **96**:15–53.
30. Den Toonder JMJ, Nieuwstadt FTM. Reynolds number effects in a turbulent pipe flow for low to moderate Re. *Physics of Fluids* 1997; **9**:3398–3409.
31. Orlandi P, Fatica M. Direct simulations of turbulent flow in a pipe rotating about its axis. *Journal of Fluid Mechanics* 1997; **343**:43–72.
32. Dong YH, Lu XY, Zhuang LX. Large eddy simulation of turbulent channel flow with mass transfer at high-Schmidt numbers. *International Journal of Heat and Mass Transfer* 2003; **46**:1529–1539.
33. Wang L, Lu XY. An investigation of turbulent oscillatory heat transfer in channel flows by large eddy simulation. *International Journal of Heat and Mass Transfer* 2004; **47**:2167–2172.


 

34. Dong YH, Lu XY. Large eddy simulation of a thermally stratified turbulent channel flow with temperature oscillation on the wall. *International Journal of Heat and Mass Transfer* 2004; **47**:2109–2122.
35. Mansour NN, Kim J, Moin P. Reynolds-stress and dissipation-rate budgets in a turbulent channel flow. *Journal of Fluid Mechanics* 1988; **194**:15–44.
36. Kristoffersen R, Andersson HI. Direct simulations of low-Reynolds-number turbulent flow in a rotating channel. *Journal of Fluid Mechanics* 1993; **256**:163–197.
37. Rubinstein R, Zhou Y. The dissipation rate transport equation and subgrid-scale models in rotating turbulence. *ICASE Report No.* 97–63, NASA/CR-97-206250, 1997.
38. Moin P, Kim J. Numerical investigation of turbulent channel flow. *Journal of Fluid Mechanics* 1982; **118**: 341–377.

 